Positioning Based on Tightly Coupled Multiple Sensors: A Practical Implementation and Experimental Assessment

3 authors:

Gianluca Falco
Istituto Superiore Mario Boella (ISMB)
56 PUBLICATIONS   **724** CITATIONS

SEE PROFILE

Mario Nicola
Istituto Superiore Mario Boella (ISMB)
47 PUBLICATIONS   **413** CITATIONS

SEE PROFILE

Marco Pini
Istituto Superiore Mario Boella (ISMB)
93 PUBLICATIONS   **1,161** CITATIONS

SEE PROFILE

Some of the authors of this publication are also working on these related projects:

ASSIST View project

ERICA Project View project

Positioning Based on Tightly Coupled Multiple Sensors: a Practical Implementation and Experimental Assessment

Gianluca Falco[1], Mario Nicola[1*], Marco Pini[1]

[1]Istituto Superiore Mario Boella, Turin, 10138 IT

Corresponding author: Mario Nicola (e-mail:nicola@ismb.it).

ABSTRACT During the last decade, the number of applications for land transportation that depend on systems for accurate positioning has significantly increased. Unfortunately, systems based on low cost Global Navigation Satellite System (GNSS) components harshly suffer signal impairments due to the environment surrounding the antenna, but new designs based on deeper data fusion and on the combination of different signal processing techniques can overcome limitations without the introduction of expensive components. Supported by a complete mathematical model, this paper presents the design of a real-time positioning system that is based on the tight integration of extremely low-cost sensors and a consumer-grade GPS receiver. The design has been validated experimentally through a series of tests carried out in real scenarios. The performance of the new system is compared against a standalone GNSS receiver and a "survey grade" professional equipment. The results show that a carefully designed and constrained integration of low-cost sensors can have performance comparable to that of an expensive professional equipment.

INDEX TERMS Global Positioning System (GPS), Inertial Navigation System (INS), position accuracy, tight architecture

I. INTRODUCTION

THE accurate and reliable estimate of vehicles position is at the basis of many applications for land transportation, but is becoming an important requirement also in other domains, such as in precision farming for the control of driverless machineries. As many scientists have pointed out in the recent years, there is an increasing demand for sub-meter position accuracy in most of operational conditions. Developers keep seeking innovative strategies and reliable systems at affordable costs [1]-[3]. Although the Global Positioning System (GPS) - in general terms, the Global Navigation Satellite System (GNSS) - remains the main mean for absolute positioning and outdoor navigation, the urban environment and specific conditions often pose severe challenges to the receivers. In fact, the presence of buildings and trees might induce signal reflections and attenuations that, in turn, cause corrupted GNSS measurements. Even worse, in severe cases, the number of visible satellites can be not sufficient, and receivers might be unable to provide Position Velocity and Time (PVT) data.

Apart from the GNSS-evolution (new constellations help to increase the satellites visibility and offer signals at different frequencies), today is already a common practice the integration of satellite navigation receivers with terrestrial sensors, namely wheel odometers [4], Inertial Navigation Systems (INSs) [5]-[7] and Light Detection and Ranging (LIDAR) [8]. Several types of integration approaches can be adopted [9], but from a general perspective they can be grouped in three main categories: the loosely coupled [10], the tightly coupled [11] and the ultra-tight integration [12], [13]. In a nutshell, the basic difference between them is the type of data shared by the GNSS receiver and the sensors. For instance, in INS/GPS loosely coupled architectures, positions and velocities estimated by the GNSS receiver are blended with the INS navigation solution. Tightly coupled architectures perform a deeper data fusion, as the estimated GNSS pseudoranges and Doppler shifts are processed through a Kalman Filter (KF) along with the INS measurements. Compared to the loosely coupled, tight integrations allow for providing PVT data even in scenarios with poor signal quality and limited satellites coverage, thanks to the prediction of pseudoranges and Doppler trends. Ultra-tight integrations, which enhance performance of less complex methods in high dynamic or weak signal conditions [14] -[16], involve the baseband signal processing of GNSS receivers, which is typically not accessible when using commercial low-cost modules.

The performance achievable with the aforementioned kinds of integration is limited by the approximations of the linearization process of the KF and the difficult characterization of the sensors errors, which is especially critical for low-cost MEMS-based IMUs [17]. In literature many solutions have been proposed to overcome such problems. KF can be replaced by Unscented Kalman Filters (UKF)[18], Particle Filtering (PF) [17], [19], [20] or several kinds of Artificial Neural Networks (ANN) [21], [22], [23], whereas the introduction of an H∞ filter can keep the KF

stable regardless of the complexity of the IMU measurements noise [24], [25]. All these solutions are characterized by a high complexity in the design of the system, which makes them unsuitable when the use of low-cost components is addressed.

This paper starts from a conventional tightly coupled architecture and presents the design of add-on algorithms, necessary to achieve a real-time implementation based on a low-cost Inertial Measurement Unit (IMU), a consumer-grade GPS receiver and odometer data available on the car Controller Area Network (CAN)-bus. The paper shows the results obtained from a set of tests performed in a real environment and compares the performance of the positioning system under test with commercial products. Although many papers describe integrated INS/GPS schemes for automotive applications (see for example [26]-[28]), very few works [29], [30] focus on the performance achievable by a tightly coupled architecture fusing measurements of extremely low-cost sensors.

Section II recalls the theory behind conventional tightly coupled architectures, while Section III accurately describes the logical controls and constraints designed for the proposed real-time implementation. These make the system robust to GNSS signal impairments and lead to performance comparable to that of a professional, dual frequency GPS receiver, combined with a tactical-grade IMU. Section IV includes a detailed description of the experimental setup, presents the methodology followed during the data post-processing and comments the results of the tests.

II. BASICS ON INS/GPS TIGHT INTEGRATION

The INS/GPS data fusion is commonly performed through a KF [31]-[33], that can be considered the reference method to perform multiple sensors data fusion [3], [11] and [34]. In a tight integration, the KF is fed by the measure of pseudoranges and pseudorange rates to assist the INS in the estimate of the user's position and velocity. The tight integration is able to aid the inertial sensors even during limited GPS satellite availability [19]. Many works related to Kalman-based tight integrations have been published in the course of the last decade, such as [3], [11], [35]-[40].

A simple diagram showing the main operations of a tight INS/GPS integration is depicted in Fig. 1.
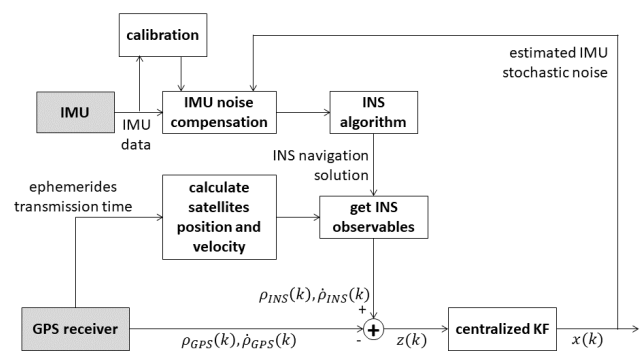

Fig. 1. Block diagram of a conventional INS/GPS tightly coupled architecture.

The block labeled as *INS algorithm* calculates the position, velocity and attitude (i.e.: the *INS navigation solution*) by exploiting the accelerometers and gyroscopes measures provided by the Inertial Measurement Unit (IMU). See [5], [11] for details.

In parallel, the *GPS receiver* provides raw measurements (i.e. code-based pseudorange, Doppler and carrier-phase measures), *ephemeris* and Position, Velocity and Time (PVT) data. The algorithm described hereafter uses GPS code-based measurements only.

Similarly, to the GPS, it is also possible to compute pseudoranges and pseudorange rates from the user's position and velocity estimated by the *INS algorithm.* At time *k,* the misclosure vector $\mathbf{z}(k)$ can be written as:

$$\mathbf{z}(k) = \begin{bmatrix} \boldsymbol{\rho}_{INS}(k) - \boldsymbol{\rho}_{GPS}(k) \\ \dot{\boldsymbol{\rho}}_{INS}(k) - \dot{\boldsymbol{\rho}}_{GPS}(k) \end{bmatrix} \qquad (1)$$

where:

$\boldsymbol{\rho}_{INS}$, $\boldsymbol{\rho}_{GPS}$ are the vectors of pseudoranges related to the INS and the GPS receiver, respectively;

$\dot{\boldsymbol{\rho}}_{INS}$, $\dot{\boldsymbol{\rho}}_{GPS}$ are the vectors of pseudoranges rates related to the INS and the GPS receiver, respectively.

The centralized KF uses as input the misclosure vector, when available, otherwise it provides an estimate of its states $\mathbf{x}(k)$ by prediction only.

For the sake of simplicity, from this moment on, the *k*-th discrete time instant is indicated by the subscript *k*. As far as the discrete time states vector of a *centralized KF* is concerned, the non-linear state transition model (system or motion model) is given by (2):

$$\mathbf{x}_k = f(\mathbf{x}_{k-1}, \mathbf{u}_{k-1}, \mathbf{w}_{k-1}) \qquad (2)$$

where $\mathbf{u}$ is the control input and $\mathbf{w}$ is the process noise.

The state measurement model is:

$$\mathbf{z}_k = h(\mathbf{x}_k, \mathbf{v}_k) \qquad (3)$$

where $\mathbf{v}_k$ is the measurement noise, which is independent of the past and current states and accounts for errors on GPS measurements. Eqs (2) and (3) can be rewritten as:

$$\delta\dot{\mathbf{x}}_k = \mathbf{F} \cdot \delta\mathbf{x}_k + \mathbf{G} \cdot \mathbf{W}_k \qquad (4)$$

where $\mathbf{F}$ is the whole matrix of the system model and $\mathbf{G}$ is the matrix that relates the states with noise sources.

$$\mathbf{z}_k = \mathbf{H} \cdot \delta\mathbf{x}_k + \mathbf{v}_k \qquad (5)$$

where $\mathbf{H}$ is the matrix that relates the states with the measurements. Eqs (4) and (5) can be tailored for the INS/GPS integration and their mathematical expression can be found in Appendix I and Appendix II, respectively.

In integrated INS/GPS systems, the required states to be estimated include the navigation parameters (i.e., positions, velocities, and attitudes) and the sensor parameters (i.e., biases and scale factors) [41]. In particular, the centralized KF is in charge of estimating the error (i.e. $\delta\mathbf{x}$) of the navigation solution, rather than the states themselves (i.e. $\mathbf{x}$) [17]. Due to the non-linear relationship between the states and the measurements the centralized KF is replaced by an Extended Kalman Filter (EKF). A typical error states vector used in case of an INS/GPS tightly coupled architectures is indicated in (6):

$$\delta\mathbf{x} = \begin{bmatrix} \delta\mathbf{r}_{3\times1}^e & \delta\mathbf{v}_{3\times1}^e & \delta\mathbf{A}_{3\times1}^e & \delta\mathbf{f}_{3\times1}^b & \delta\boldsymbol{\omega}_{3\times1}^b & \delta b_r & \delta d_r \end{bmatrix}^T \qquad (6)$$

where

$\delta\mathbf{r}_{3\times1}^e$ is the position error vector;

$\delta\mathbf{v}_{3\times1}^e$ is the velocity error vector;

$\delta\mathbf{A}_{3\times1}^e$ is the attitude error vector;

$\delta\mathbf{f}_{3\times1}^b$ is the error vector related to the specific forces measured by the IMU in the body frame '*b*';

$\delta\boldsymbol{\omega}_{3\times1}^b$ is the error vector related to the angular rates measured by the IMU in the body frame '*b*';

δb_r is the receiver's clock bias;

δd_r is the receiver's clock drift.

By applying the perturbation analysis [5], an INS error model can be derived to represent the dynamics of the navigation error states (i.e. $f()$, according to (2)). For ease of comprehension, the calculation of such matrix, both in continuous and discrete-time, is reported in Appendix I, while Appendix II describes the mathematical relationship between measurements and states in case of an INS/GPS tightly coupled integration.

III. ADVANCED INS/GPS TIGHT INTEGRATION FOR PRACTICAL IMPLEMENTATION

In the proposed system, the performance of the traditional INS/GPS tight integration has been improved through the exploitation of additional constraints and ad-hoc strategies, inspired by the knowledge of the final application of the positioning system. This improvement has been obtained by focusing on four main aspects:

A. reduction of the tightly coupled EKF divergence during long GPS signal outages;
B. countermeasures to the initial large heading error that can lead to filter instability;
C. limitation of the INS errors drift within the navigation solution;
D. monitoring of the measurements quality and validity of the code-based GPS measurements.

Each aspect is discussed in the following subsections.

A. Reduction of the tightly coupled EKF divergence during long GPS signal outages

During GPS signal outages, the tight integration calculates the position with the IMU data and skips the update phase due to the absence of GPS measurements. In such conditions, low-cost MEMS-based IMUs can lead to a remarkable degradation in terms of positioning accuracy even after a short amount of time. In order to overcome this problem, the output of an odometer and two Non-Holonomic Constraints (NHC) [3] are added to the system. Exploiting this information, the update phase of the EKF can be performed also during GPS signal outages. The block diagram of this enhancement is depicted in Fig. 2 with bold lines.
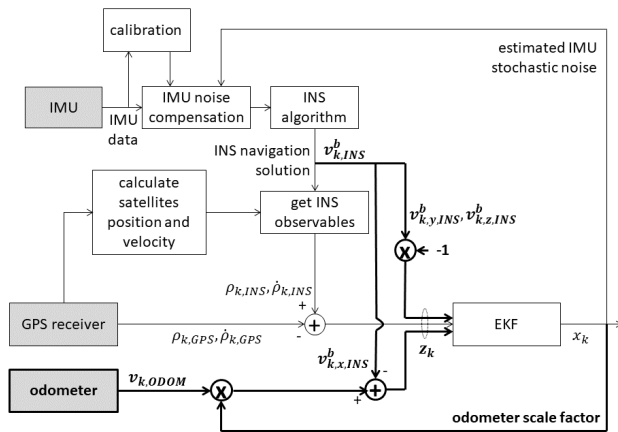

Fig. 2. Block diagram of a GPS/INS tightly coupled architecture enhanced by NHC constraints and odometer measurements.

The measurements misclosure equation is expressed in (7):

$$\mathbf{Z}_{k,OUTAGE} = \left[\begin{pmatrix} S \cdot \mathrm{v}_{ODOM} \\ 0 \\ 0 \end{pmatrix} - \left(\mathbf{R}_{b,3\times3}^{e} \right)^{T} \cdot \mathbf{v}_{INS,3\times1}^{e} \right] \quad (7)$$

where:

S is the odometer scale factor;

v_{ODOM} is the velocity of the odometer computed with respect to the vehicle's frame;

$\mathbf{R}_{b,3\times3}^{e}$ is the direction cosine matrix from the body frame '*b*' to ECEF frame '*e*';

$\mathbf{v}_{INS,3\times1}^{e}$ is the velocity vector of the vehicle computed through the INS algorithm in the ECEF frame.

Since the scale factor S of the odometer is taken into account, an additional error state needs to be included in the vector $\delta \mathbf{x}$ as expressed in (6). Thus, leveraging on (2), the INS/GPS system model as described in (4) is augmented as:

$$\begin{bmatrix} \delta \dot{\mathbf{x}}_{INS/GPS} \\ \delta \dot{S} \end{bmatrix} = \underbrace{\left[\begin{array}{ccccccc|c} & & & \mathbf{F}_{INS/GPS,17\times17} & & & & \mathbf{0}_{17\times1} \\ \hline \mathbf{0}_{1\times3} & \mathbf{0}_{1\times3} & \mathbf{0}_{1\times3} & \mathbf{0}_{1\times3} & \mathbf{0}_{1\times3} & 0 & 0 & 0 \end{array} \right]}_{\substack{\mathbf{F} \\ INS/GPS/ODOM,18\times18}} \cdot \underbrace{\begin{bmatrix} \delta \mathbf{x}_{INS/GPS} \\ \delta S \end{bmatrix}}_{\substack{\delta \mathbf{x} \\ INS/GPS/ODOM,18\times1}}$$

$$+ \underbrace{\left[\begin{array}{cccc} & \mathbf{G}_{INS/GPS,17\times14} & & \\ \mathbf{0}_{1\times3} & \mathbf{0}_{1\times3} & 0 & 0 \end{array} \right]}_{\substack{\mathbf{G} \\ INS/GPS/ODOM,18\times14}} \cdot \mathbf{W}_{INS/GPS} \quad (8)$$

where $\delta \mathbf{x}_{INS/GPS}$, $\mathbf{F}_{INS/GPS}$, $\mathbf{G}_{INS/GPS}$, and $\mathbf{W}_{INS/GPS}$ are the error states vector, the system model matrix, the matrix that relates the dynamic model to its noise sources, and the noise process vector as expressed in (6) and (4), respectively. The discrete-time version of (8) can be obtained by following the procedure reported in Appendix I.

Eventually, the new discrete-time design matrix $\mathbf{H}_{k,OUTAGE}$ that relates the measurements with the error states of the EKF in case of GPS signal outage is obtained through perturbations of (7), both for $\delta \begin{pmatrix} S \cdot \mathrm{v}_{ODOM} \\ 0 \\ 0 \end{pmatrix}$ and $\delta \left[\left(\mathbf{R}_{b,3\times3}^{e} \right)^{T} \cdot \mathbf{v}_{INS,3\times1}^{e} \right]$, according to [42]. The solution can be summarized as:

$$
\underbrace{\begin{bmatrix} S \cdot v_{ODOM} \\ 0 - v^b_{y,INS} \\ 0 - v^b_{z,INS} \end{bmatrix}}_{\substack{\mathbf{Z}_k \\ OUTAGE}} = \underbrace{\begin{bmatrix} \mathbf{0}_{1\times3} & 0_{1\times8} & -v_{WSS} \\ \mathbf{0}_{1\times3} & \mathbf{N}_{HC,3\times6} & 0_{1\times8} & 0 \\ \mathbf{0}_{1\times3} & 0_{1\times8} & 0 \end{bmatrix}}_{\substack{\mathbf{H}_k \\ OUTAGE}} \cdot \delta\mathbf{x}_{k,18\times1} + \mathbf{v}_{k,3\times1} \tag{9}
$$

where

$v^b_{y,INS}$, $v^b_{z,INS}$ are the INS velocities estimation along the Y and Z axes, expressed in the body frame. They are obtained from $\left(\mathbf{R}^e_{b,3\times3} \right)^T \cdot \mathbf{v}^e_{INS,3\times1}$ product;

$\mathbf{N}_{HC,3\times6}$ is the non-holonomic matrix, whose definition is omitted for sake of simplicity and can be found in [3] and [42];

$\mathbf{v}_{k,3\times1}$ is the noise vector associated to the constraints. Its covariance matrix can be described as a 3x3 diagonal matrix whose elements on the diagonal can be assumed to have a Gaussian distribution as $\mathbf{v}_{k,3\times1} \sim N(\mathbf{0}, \mathbf{\gamma}_{3x3,\mathbf{v}_k})$.

B. Countermeasures to the initial large heading error

As correctly explained in [43], in low-cost INS/GPS navigation systems, the poor performance of the gyros makes an accurate initialization of the heading angle difficult. Different approaches have been proposed to overcome such issue, e.g. in [43], [44], and [45], but they imply strong modifications of the INS/GPS-integration architecture and an increment in the system complexity.

In order to implement minimum changes in the conventional tightly coupled algorithm, we introduced an additional constraint based on the Course Over Ground (COG) that can be calculated from the GPS receiver estimated velocities as:

$$
\psi_{GPS} = \tan^{-1}\left(\frac{V^n_{East,GPS}}{V^n_{North,GPS}} \right) \tag{10}
$$

where ψ_{GPS} is the heading angle derived from the GPS velocity and the superscript 'n' indicates that such GPS velocities are measured with respect to the local frame. The transformation of the GPS velocity vector from the ECEF frame to the local frame can be obtained as in the following:

$$
\mathbf{V}^n_{GPS} = \mathbf{R}^n_e \cdot \mathbf{V}^e_{GPS} \tag{11}
$$

where $\mathbf{R}^n_e$ is the rotation matrix from the ECEF to the local frame whose mathematical expression can be found in [5].

The use of the COG constraints is limited by the quality of

the ψ_{GPS} estimation, which is reliable only when the vehicle is moving. The detection of the vehicle's dynamic condition is obtained by checking the condition $\left\| \mathbf{V}^n_{GPS} \right\| \geq \ell$, where ℓ is the minimum acceptable velocity. A block diagram that shows the COG constraint is illustrated in Fig. 3, with bold lines.
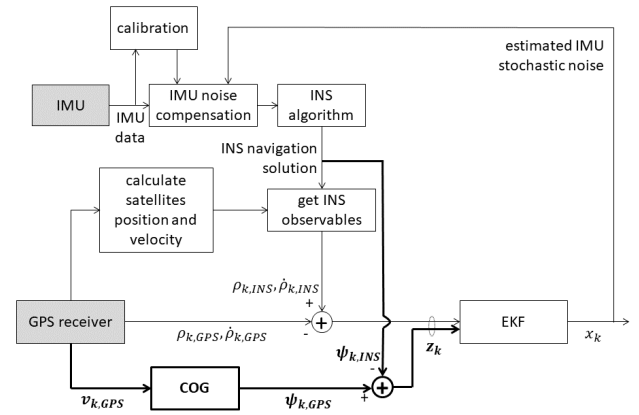

Fig. 3. Block diagram of a GPS/INS tightly coupled architecture enhanced by Course Over Ground (COG) constraint.

Such constraint does not modify the system model of the EKF tightly coupled architecture, described in (8), but only the measurements misclosure and the design matrix. The general relationship between the measurement and the error states as in (3) can be expanded and tailored to the GPS/INS integration as in (5) and further augmented to include the COG constraints:

$$
\underbrace{\begin{bmatrix} \mathbf{Z}_{k,INS/GPS} \\ \psi_{k,GPS} - \psi_{k,INS} \end{bmatrix}}_{\substack{\mathbf{Z}_k \\ INS/GPS/COG}} = \underbrace{\begin{bmatrix} \mathbf{H}_{k,INS/GPS} \\ \mathbf{0}_{1\times3} & \mathbf{0}_{1\times3} & \frac{\delta\hat{\psi}}{\delta A_x} & \frac{\delta\hat{\psi}}{\delta A_y} & \frac{\delta\hat{\psi}}{\delta A_z} & 0_{1\times9} \end{bmatrix}}_{\substack{\mathbf{H}_k \\ INS/GPS/COG}} \cdot \delta\mathbf{x}_{k,18\times1} + \mathbf{v}_k \tag{12}
$$

where

$\mathbf{Z}_{k,INS/GPS}$, $\mathbf{H}_{k,INS/GPS}$ are the measurements vector and the design matrix of the reference EKF tightly coupled algorithm at the k-th time instant as stated in (5);

$\psi_{k,GPS}$ is the heading angle computed through (10);

$\psi_{k,INS}$ is the heading angle computed from the INS algorithm;

$\frac{\delta\hat{\psi}}{\delta A_x}$, $\frac{\delta\hat{\psi}}{\delta A_y}$, $\frac{\delta\hat{\psi}}{\delta A_z}$ are the partial derivatives of the heading error computed with respect to the attitude along the X, Y, Z axes of the ECEF frame. Details on the calculation of these derivatives can be found in [3].

C. Limitation of the INS errors drift

The general IMU error model reported in [11] loses validity when extremely inexpensive IMUs are used [49]. According to [50], a more comprehensive error model includes four error

components: a fixed contribution, a temperature-dependent variation, a run-to-run variation, and an in-run variation. The following subsections present the strategies adopted to mitigate the effects of in-run and run-to-run variations, as well as the temperature compensation. The fixed contribution (e.g. bias) can easily be evaluated and corrected though a proper calibration process and it is omitted in this paper.

C1. In-run compensation

The in-run variation is the component that mostly affects the performance of an MEMS IMU and includes the IMU errors variation over time: consequently, this kind of errors cannot be corrected during the initial calibration or the system alignment.

Since the presented tightly coupled system is targeted to land applications, a recalibration can be performed every time the vehicle is still and the deterministic gyros bias vector $\mathbf{d}$ can be updated. The static condition of the user can be precisely detected by checking the velocity from the odometer or the velocity evaluated by the GPS receiver, $\left\| \mathbf{V}_{GPS}^{n} \right\| \sim 0$.

The recalibration of gyroscopes reduces the effects of the in-run variations of IMU errors. A further reduction can be accomplished by adding two additional constraints during the static conditions. The Zero Velocity Update (ZUPT) measurements [51] limits the effects of the accelerometers errors on the velocity estimates and, consequently, on the position, while a Zero Integrated Heading Rate (ZIHR) approach [52] is adopted to mitigate the growth of the heading error due to residual gyroscopes errors. A block diagram that depicts the strategies adopted in case of static conditions of the vehicle is shown in Fig. 4 and highlighted by bold lines.
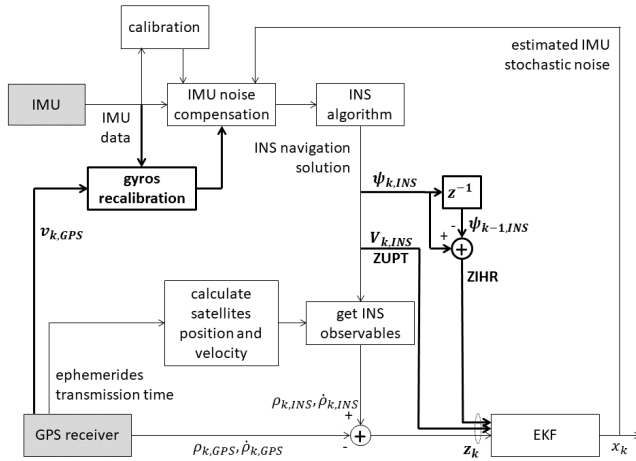

Fig. 4. Block diagram of a GPS/INS tightly coupled architecture enhanced with ZUPT/ZIHR constraints and gyros recalibration during static condition.

In details, the ZUPT constraint can be included within the INS/GPS measurements misclosure vector (reported in 5 according to (3)) as:

$$\underbrace{\begin{bmatrix} \mathbf{Z}_{k,INS/GPS} \\ \mathbf{V}_{k,INS}^{e} - \mathbf{0} \end{bmatrix}}_{\substack{\mathbf{Z}_k \\ ZUPT}} = \underbrace{\begin{bmatrix} \mathbf{H}_{k,INS/GPS} \\ \hline \mathbf{0}_{3\times3} & \mathbf{I}_{3\times3} & \mathbf{0}_{1\times12} \end{bmatrix}}_{\substack{H_k \\ ZUPT}} \cdot \delta \mathbf{x}_{k,18\times1} + \mathbf{v}_k \quad (13)$$

where $\mathbf{V}_{k,INS}^{e}$ is the velocity estimated through the INS algorithm and expressed in the ECEF frame.

The ZIHR can be written as:

$$\underbrace{\begin{bmatrix} \mathbf{Z}_{k,INS/GPS} \\ \psi_{k,INS} - \psi_{k-1,INS} \end{bmatrix}}_{\substack{\mathbf{Z}_k \\ ZIHR}} = \underbrace{\begin{bmatrix} \mathbf{H}_{k,INS/GPS} \\ \hline \mathbf{0}_{1\times3} & \mathbf{0}_{1\times3} & \mathbf{0}_{1\times3} & \mathbf{0}_{1\times3} & \mathbf{M}_{ZIHR,1\times3} & \mathbf{0}_{1\times3} \end{bmatrix}}_{\substack{H_k \\ ZIHR}} \cdot \delta \mathbf{x}_{k,18\times1} + \mathbf{v}_k \quad (14)$$

where

$\psi_{k,INS}, \psi_{k-1,INS}$ are the heading angle computed through the INS algorithm as in (1) at the *k*-th and *k-1*-th time instants, from the INS algorithm;

$\mathbf{M}_{ZIHR,1\times3}$ is equal to $\begin{bmatrix} 0 & \sec\theta\sin\varphi & \sec\theta\cos\varphi \end{bmatrix}$ where φ, θ, are the roll and pitch angles, respectively. They are assumed to be constant during the time interval Δt_k.

C2.   Run-to-run compensation

The run-to-run bias (also called turn-on bias) is the bias in the inertial sensor output when the sensor is turned on. In most of the high-end, navigation-grade, IMUs, the turn-on biases do not change in a significant way among different missions and it can be considered negligible [3]. However, for low cost sensors these errors are quite large, and their repeatability is typically poor, asking for frequent calibrations.

The recalibration procedure, introduced in Section III.C.1, is feasible for the gyroscopes but is impractical for the accelerometers. The method we used to overcome such issue includes extra states in the EKF, which are in charge of estimating the turn-on bias components for both the gyroscopes and the accelerometers. Therefore, the error states vector described in (8) can be further expanded to a 24-element vector and the new transition matrix can be written in continuous-time as:

$$
\begin{bmatrix} \delta\dot{\mathbf{x}}_{INS/GPS/ODOM,18\times1} \\ \delta\boldsymbol{\tau}_{f,3\times1} \\ \delta\boldsymbol{\tau}_{\omega,3\times1} \end{bmatrix} = \underbrace{\begin{bmatrix} \mathbf{F}_{INS/GPS/ODOM,18\times18} & \mathbf{0}_{3\times3} & \mathbf{0}_{3\times3} \\ \mathbf{0}_{3\times3} & \cdots & \mathbf{0}_{3\times3} & \mathbf{0}_{3\times3} \\ \mathbf{0}_{3\times3} & \cdots & \mathbf{0}_{3\times3} & \mathbf{0}_{3\times3} \end{bmatrix}}_{\substack{\mathbf{F} \\ TURN-ON\ BIASES,24\times24}} \cdot \underbrace{\begin{bmatrix} \delta\mathbf{x}_{INS/GPS/ODOM,18\times1} \\ \delta\boldsymbol{\tau}_{f,3\times1} \\ \delta\boldsymbol{\tau}_{\omega,3\times1} \end{bmatrix}}_{\substack{\delta\mathbf{x} \\ TURN-ON\ BIASES,24\times1}}
$$

$$
+ \underbrace{\begin{bmatrix} \mathbf{G}_{INS/GPS/ODOM,18\times14} \\ \mathbf{0}_{3\times3} & \mathbf{0}_{3\times3} & \mathbf{0}_{3\times1} & \mathbf{0}_{3\times1} \\ \mathbf{0}_{3\times3} & \mathbf{0}_{3\times3} & \mathbf{0}_{3\times1} & \mathbf{0}_{3\times1} \end{bmatrix}}_{\substack{\mathbf{G} \\ TURN-ON\ BIASES,24\times14}} \cdot \mathbf{W}_{INS/GPS}
$$

(15)
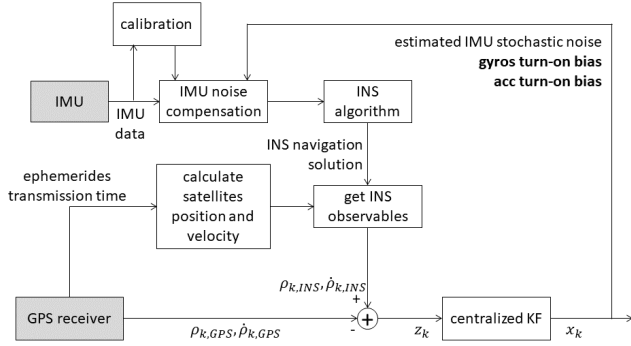

Fig. 5. Block diagram of a GPS/INS tightly coupled architecture enhanced by additional error states to comprise INS turn-on biases.

Fig. 6. Block diagram of a GPS/INS tightly coupled architecture enhanced with an additional module for IMU temperature compensation.

where $\delta\boldsymbol{\tau}_{f,3\times1}$ and $\delta\boldsymbol{\tau}_{\omega,3\times1}$ are the error states associated to the turn-on biases of the accelerometers and gyroscopes, respectively. They are expressed as constant terms over time and thus their derivatives are equal to zero. A graphical view of these changes is reported in Fig. 5 over the block diagram of the GPS/INS tightly coupled architecture.

C3. Temperature compensation

In an IMU where the gyros and accelerometers are not temperature compensated (as most of the low-cost consumer-grade MEMS IMUs), the effects of the temperature variations have a remarkable impact on the accuracy of the INS navigation solution because such temperature variations make the biases of the INS sensors changing over time. Thus, we calibrated the INS sensors in a temperature-controlled chamber, rotating the IMU in different positions according to the characterization tests proposed in [47]. We repeated the same procedure for different temperatures in the range from -20 to 60 Celsius. A similar procedure has been also adopted for the gyroscopes and the accelerometers. The collected values were included into a look-up table that was used to correct the IMU measurements in real-time. The additional module in charge of correcting the IMU biases according to the current temperature measured by the IMU is shown in Fig. 6.
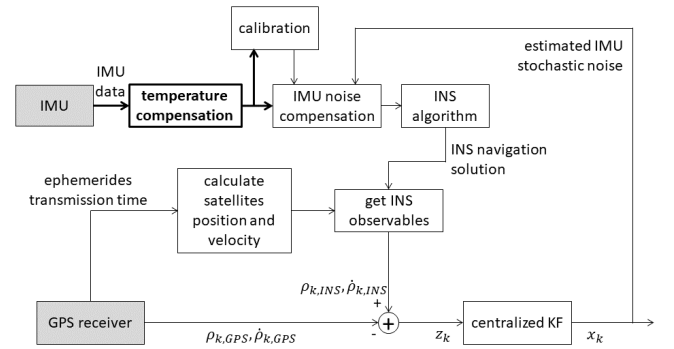
D. Monitoring of the measurements quality and validity of code-based GPS measurements

In case of harsh environments (e.g. urban, mountain areas), signal impairments can affect the quality of GNSS measurements and, consequently, the accuracy of the final system positioning. The Carrier to Noise density ratio (C/N0) [53] and the elevation of satellite allow for assessing the quality of the received signal. Indeed, the exclusion of satellites with low C/N0 (e.g. C/N0 lower than 30 dB-Hz) and those with low elevations (e.g. elevation less than 10 °) can reduce the impact of signal degradation on the position accuracy. In addition, the selected measurements can be further weighted. In details, each element of the diagonal covariance matrix $\mathbf{R}_{\mathbf{v}_k}$ that refers to a code-based GPS measurements, is computed as in (16), by following the model proposed in [53] and [54]:

$$
\sigma_\rho^2 = \frac{\left(a + b \cdot 10^{-\frac{C}{N_0}} \right)}{\sin\left(Elev \right)}
$$

(16)

where $Elev$ is the satellite elevation and a, b are empirical parameters that change according to the environmental

scenario [54]. A method to select the scenario can be implemented by using an embedded map, or, more easily, by evaluating the estimated velocity of the receiver [1].

Another problem that sometimes plagues the accuracy of the tightly coupled navigation solution is the validity of the GPS data. In order to limit such issue, we implemented a method to reject the corrupted measurements, similarly to that proposed in [55]. The absolute value of a code-based pseudorange is compared with the predicted geometrical distance. Leveraging on (5), the validity check of the GPS measurements at the k-th time instant can be expressed as:

$$\left| (\boldsymbol{\rho}^i_{k,GPS} - \mathbf{H}^i_{\rho,1\times3} \cdot \delta\mathbf{x}^-_{k,3\times1}) \right| < \lambda_{MAX} \qquad (17)$$

where:

i is the index related to the satellite under investigation;

$\boldsymbol{\rho}^i_{k,GPS}$ represents the GPS code-based pseudorange associated to the i-th satellite;

$\mathbf{H}^i_{\rho,1\times3}$ is the design matrix related to the i-th satellite;

$\delta\mathbf{x}^-_{k,3\times1}$ is the vector of the vehicle position obtained through the EKF prediction stage [31];

λ_{MAX} is the maximum acceptable pseudorange error. The value of the threshold has been set empirically (e.g. twice the standard deviation of the User Equivalent Range Errors (UERE) [3]).
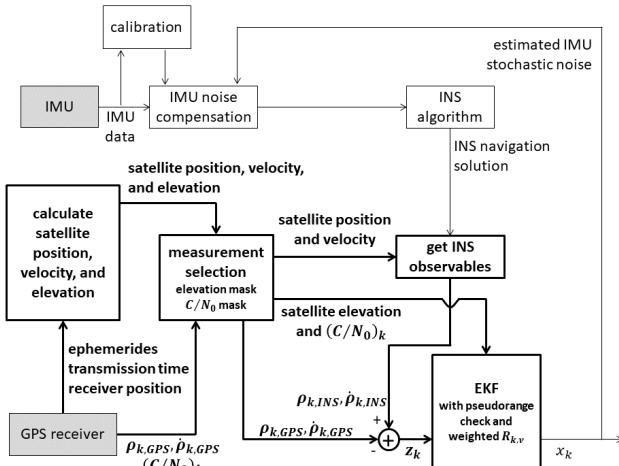

Fig. 7. Block diagram of a GPS/INS tightly coupled architecture enhanced by an additional module for GPS data validity and quality monitoring.

When invalid pseudoranges are encountered, all the measurements related to the corresponding satellites are not included in the computation of states and covariance updates. Fig. 7 shows how the conventional architecture changes with this additional strategy to check the quality and validity of the received GPS data.

IV. EXPERIMENTAL VALIDATION
A. Embedded board used for the implementation

The designed architecture was implemented on the embedded system reported in Fig. 8 that provided real time PVT data.
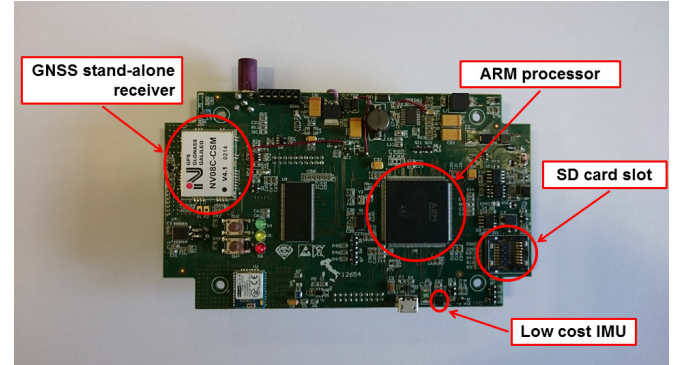

Fig. 8. View of the embedded system running the tightly coupled algorithm. The main sensors and the microcontroller are highlighted.

In summary, the board is composed of the following major components:

- a consumer-grade MEMS IMU (i.e. the InvenSense MPU-9250);
- a GPS mass-market module (i.e. the NVS NV08C-CSM);
- a 200MHz ARM micro-controller manufactured by ST-MicroElectronics (i.e. the STM32F745IET6), running FreeRTOS as the operating system;
- vehicle odometric readings in form of pulses.

The performance of the system was assessed through several tests carried out in real scenarios, following the methodology and the set up described in the next sections.

B. Experimental test setup

The developed system was mounted on board of a vehicle. For the sake of comparison, during the tests, additional positioning sensors were used in parallel to have benchmark measurements. In details, the following commercial modules were installed along with the system under test:

- a standalone, multi-constellations GNSS receiver (i.e.: NVS NV08C-CSM), not augmented by INS and odometry data. Such a GNSS receiver is commonly used in consumer-grade devices for road navigation. It was taken as a benchmark to quantify the benefits introduced by the INS and the odometer to cope with poor GNSS performance (i.e.: few satellites in view, degraded GNSS measurements due to the local environment).

- a dual-frequency, survey-grade GNSS receiver, combined with a tactical-grade inertial sensor (i.e.: Novatel SPAN-CPT). This is able to provide sub-decimeter position accuracy and is generally employed in professional applications. It was included in the experimental set up because it provided the reference trajectory that served to estimate the position errors of the developed system.

Fig. 9 sketches the block diagram of the whole experimental setup, where the RF signal from the antenna was split and sent to the developed system and the standalone NVS NV08C-CSM and the Novatel SPAN-CPT.
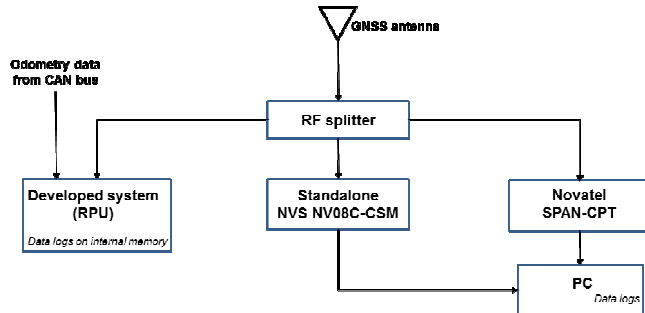

Fig. 9. Scheme of the experimental setup used to assess the performance of the developed system.

The data sets collected during the tests were logged and carefully analyzed in post-processing. The results are described in the next subsections where the acronym RPU (Robust Positioning Unit) is used to indicate the developed system running the tightly coupled algorithms. The data sets were divided in two main groups:

1. in the first, the odometer was not used and the RPU was configured to use the GNSS receiver and the IMU only. All the constraints described in Section III were enabled. In such tests, the positions and attitudes estimated by the Novatel SPAN-CPT were considered the reference both for the trajectory and for the system orientation. The results of the first group of tests are commented in Section IV.C.

2. in the second, the odometer was enabled to have an additional source of data to further increase the positioning performance. The second group of tests was characterized by long GNSS signal outages due to the presence of tunnels. Therefore, rather than the Novatel SPAN-CPT (that also showed not negligible position errors), a digital map was used as reference for the assessment of the RPU performance. The results of the second group of tests are commented in Section IV.D.

C. RPU performance in urban and open-sky scenarios

In the first group of tests, the vehicle was driven along areas with the following environmental features:

- urban areas, characterized by narrow streets surrounded by buildings and trees, limiting the visibility of the satellites and increasing the probability of GNSS signal degradation due to multipath and shadowing;
- open-sky areas, where few obstacles rarely impaired the visibility of the satellites;
- short signal outages (caused by underpasses or urban bridges) that blocked the reception of the GNSS signals.
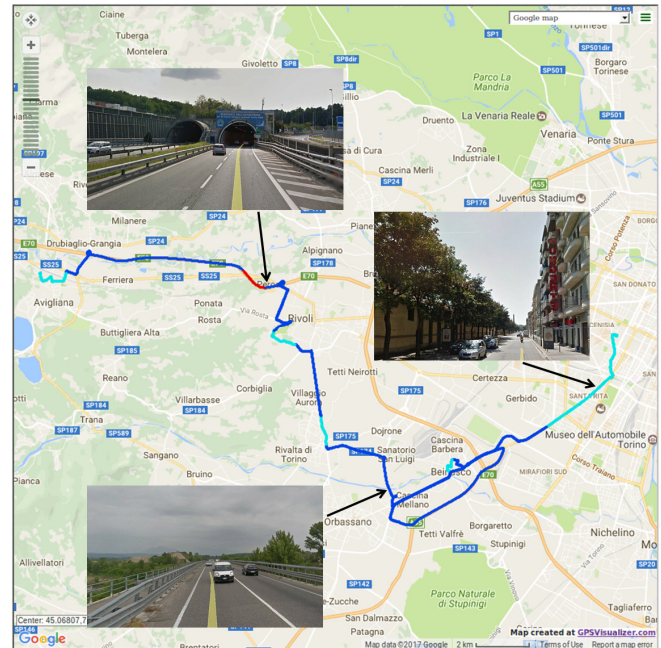

Fig. 10. Map view of the path driven during one test of the first series.

An example of a driven path is reported in Fig. 10, where the different environmental conditions are highlighted. In details, the cyan indicates the urban environment, the blue is the open-sky, while the red color indicates an outage.

As far as the performance results are concerned, the navigation solutions obtained through the RPU were compared with those provided by the benchmark standalone GNSS receiver. Fig. 11 reports the horizontal position errors over time, computed against the Novatel SPAN-CPT, where the different colors indicate again the type of environmental scenario.
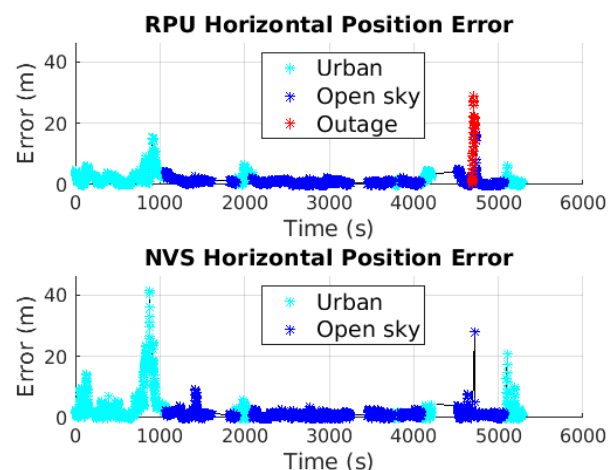

Fig. 11. Horizontal position error of the RPU (top) and of the standalone GNSS NVS receiver (bottom). Data referred to a trajectory selected as example from the first group of tests.

A thorough statistical analysis of such horizontal position errors was performed in terms of mean value, standard

deviation and 95th percentile. These metrics are calculated according to the method described in [56]. The results are reported in Table I.

TABLE I
STATISTICAL ANALYSIS OF THE HORIZONTAL POSITIONING ERRORS FOR THE NAVIGATION SYSTEMS UNDER INVESTIGATION.

Scenario	Mean value (m)		Standard deviation (m)		95th percentile (m)	
	RPU	NVS	RPU	NVS	RPU	NVS
Open-Sky	0.6	0.5	1.4	1.4	2.4	2.3
Urban	1.2	1.6	3.0	6.0	5.9	17.1
Outage	13.4	N.A.	9.8	N.A.	26.8	N.A.
Complete	0.9	0.9	2.6	3.9	4.4	5.8

From Table I, we can appreciate the benefits of the INS/GPS tightly coupled integration, in particular when the satellites visibility is poor. In urban environment, even with low cost sensors, the RPU shows a remarkable reduced error with respect to the standalone GNSS receiver, as underlined by the 95th percentile value (i.e.: it passes approximately from 17 m to 6 m). Moreover, when a signal outage occurs, the robustness of the designed architecture is further evident, as the stand-alone receiver is not able to provide any valid position during that time interval. This induces a higher availability of positioning data. As expected, only when the number of satellites in view is high, like in open-sky condition, the RPU and the standalone GNSS receiver provide similar performance (i.e.: the 95th percentile is slightly less than 2.5 m in both cases).

Fig. 12 and Fig. 13 show the two-dimensional distribution of the horizontal position error, along the East-North (EN) coordinates, for the RPU and the standalone GNSS NVS receiver, respectively.
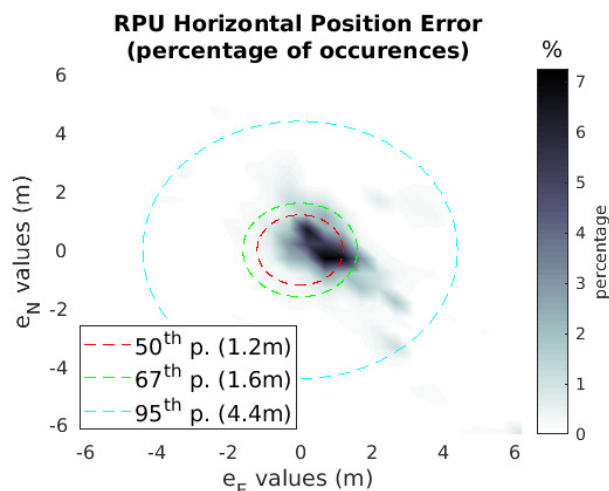

Fig. 12. Histogram of the RPU horizontal position errors. Data referred to a trajectory selected as example from the first group of tests.

From these figures it is possible to appreciate the clustering of the estimated positions errors provided by the two systems under investigation (i.e. RPU and NVS).
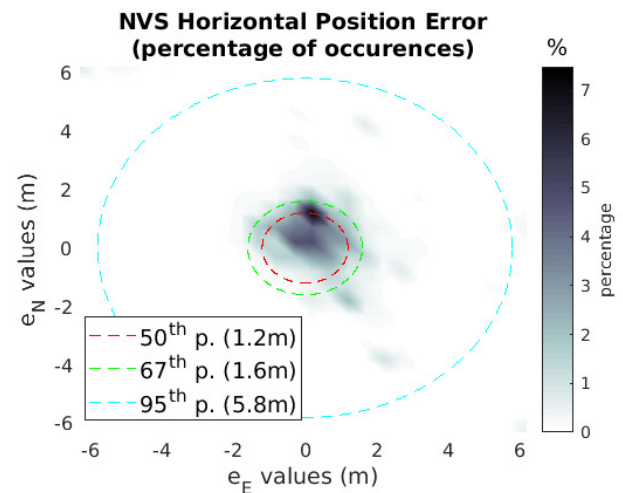

Fig. 13. Histogram of the horizontal position errors of the standalone GNSS receiver. Data referred to a trajectory selected as example from the first group of tests.

The black spots reveal the maximum density of the errors. Comparing the two figures, only a slight improvement of the RPU with respect to the standalone GNSS receiver can be observed. However, it must be noticed that the figures report the horizontal position errors computed over the whole path, which was characterized by long sections of open-sky conditions, where the two systems had similar performance.

For the sake of completeness, also the errors of the yaw estimate were calculated against the Novatel SPAN-CPT, for the RPU and the standalone GNSS receiver. These are reported in Fig. 14.
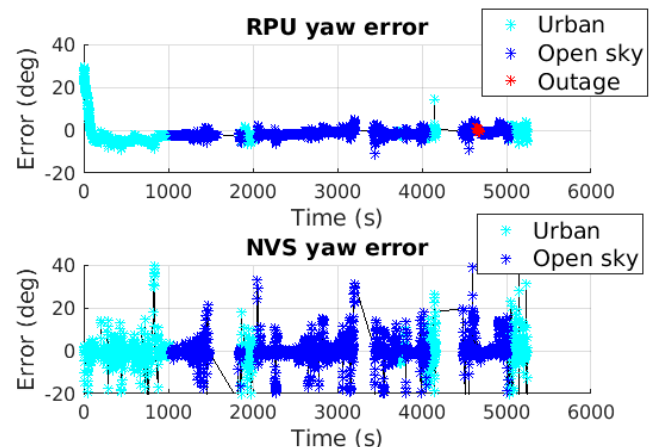
Fig. 14. Yaw angle errors over time as estimated by the RPU and the standalone GNSS receiver. Data referred to a trajectory selected as example from the first group of tests.

From Fig. 14, it is possible to observe that with the RPU most of the time the error on the yaw angle is lower than 5°. Only in the initial part of the data collection the error is high. This is due to the time required by the EKF to recover the initial large heading angle error that is related to the intrinsic features of a consumer-grade MEMS IMU. The developed system recovers such a large initial error completely, as soon

as the vehicle moves, with an estimated transient shorter than 2 minutes.

The standalone GNSS receiver shows a degraded accuracy of the estimated yaw angles that resulted strongly dependent on the speed of the vehicle, as stated in Section III.B. The higher the vehicle velocity, the more reliable the yaw angle estimate. Fig. 14 clearly shows that the trend of the yaw angles estimated by the standalone GNSS receiver is much noisier with respect to that obtained by the RPU. As done for the horizontal position errors, we computed the mean, standard deviation and 95th percentile of the errors of the estimated yaw angles, in different environmental conditions. Table 2 reports the results.

TABLE II
STATISTICAL ANALYSIS OF THE ERROR OF THE ESTIMATED YAW ANGLE FOR THE RPU AND THE STANDALONE GNSS RECEIVER.

Scenario	Mean value (deg)		Standard deviation (deg)		95th percentile (deg)	
	RPU	NVS	RPU	NVS	RPU	NVS
Open-Sky	-1.2	-0.2	1.18	5.48	2.95	14.13
Urban	-2.2	-0.1	4.28	11.2	6.36	16.18
Outage	0.32	N.A.	0.43	N.A.	1.03	N.A.
Complete	-1.5	-0.2	2.80	7.75	5.21	14.5

As expected, in an open-sky scenario, the yaw error is lower using the RPU, where the heading information coming from the IMU can be frequently constrained with that obtained by the GPS COG data. In such a scenario, the error of the heading angle is further characterized by a low standard deviation (i.e.: approximately 1.2^{o} against 5.5^{o}) and low 95th percentile (i.e.: approximately 3° against 14°). On the contrary, in an urban environment frequent car stops and low vehicle speeds are often experienced. In these cases, the GPS is not able to provide reliable COG values. Consequently, the IMU cannot leverage on the external COG and the heading angle accuracy becomes lower than that achieved in open-sky (i.e.: 2.2^{o} on average and 4.3^{o} as standard deviation).

As far as the yaw angle estimated by the benchmark receiver is concerned, higher values of the standard deviation and 95th percentile can be observed, either in open-sky and urban scenarios. In fact, the standalone GNSS receiver provides attitude estimates with a standard deviation that ranges from 5.5^{o} in case of good satellites visibility to more than 11° in an urban environment. This is almost three times bigger than the standard deviation provided by the RPU. Similarly, when the standalone GNSS receiver is used, a 95th percentile that varies from 14° to more than 16° is obtained in case of open-sky and urban scenarios, respectively. If such values are compared with those measured by the RPU in the same scenarios, an increment of almost 12° and 10° can be observed. Moreover, in case of GPS signal outage, the standalone GNSS receiver cannot provide any attitude information.

D. RPU performance in case of long GPS outages

In order to assess the improvements of the tightly coupled architecture adding data from an odometer, several tests have been carried out in a mountain environment, where the RPU had to cope with frequent long outages due to the presence of tunnels. This section reports the results obtained from two representative paths, which are depicted on the map in Fig. 15.a and in Fig. 15.b, respectively.
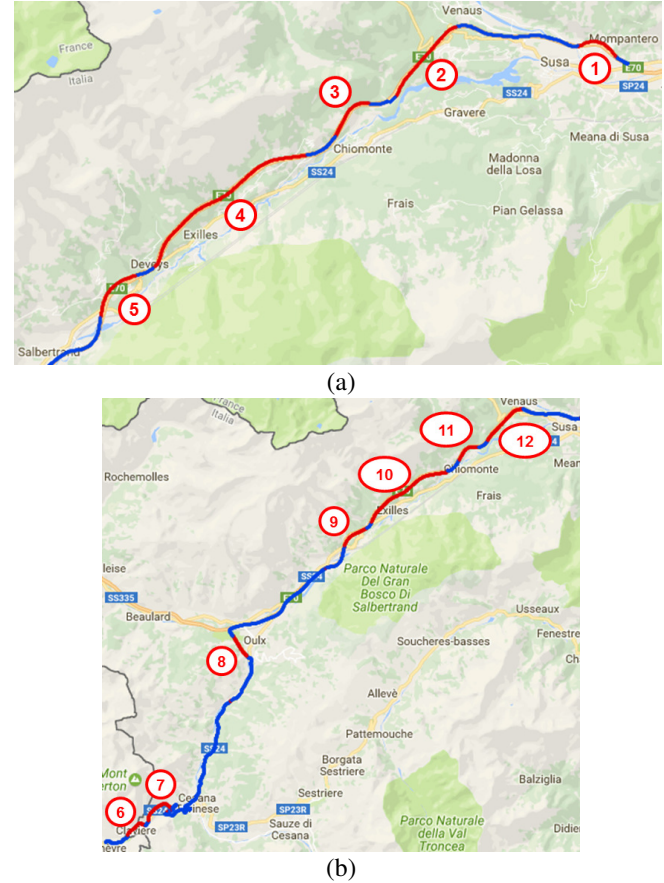

(a)

(b)

Fig. 15. Map of two paths in mountain areas. The parts of the path where GPS signals are not available due to tunnels are numbered and colored in red.

In these figures, the part of the path colored in blue indicates open-sky conditions, while the part colored in red is used to underline the presence of a tunnel. Close mountains around the road sometimes limit the visibility of the satellites and cause multipath effects on the GNSS signal. Moreover, in the figures, the encountered GNSS signal outages have been numbered from 1 to 12 and this index is used to refer to a specific tunnel.

The results reported in this section refer to a test performed with the experimental set up commented in Section IV.B, where we substituted the GNSS standalone receiver with an additional RPU. Indeed, two RPUs ran in parallel during the tests and their navigation solutions were stored and compared in post-processing. In details, the first RPU was equipped only with the INS and the GNSS receiver, while the second RPU was set to receive data also from the odometer, as described in Section III.A. In this way, it was possible to assess the advantages brought by the odometer (and the related digital processing) within the developed system.

A zoomed view of the positions stored by the two RPUs and the Novatel SPAN-CPT is reported over a map in the following figures.
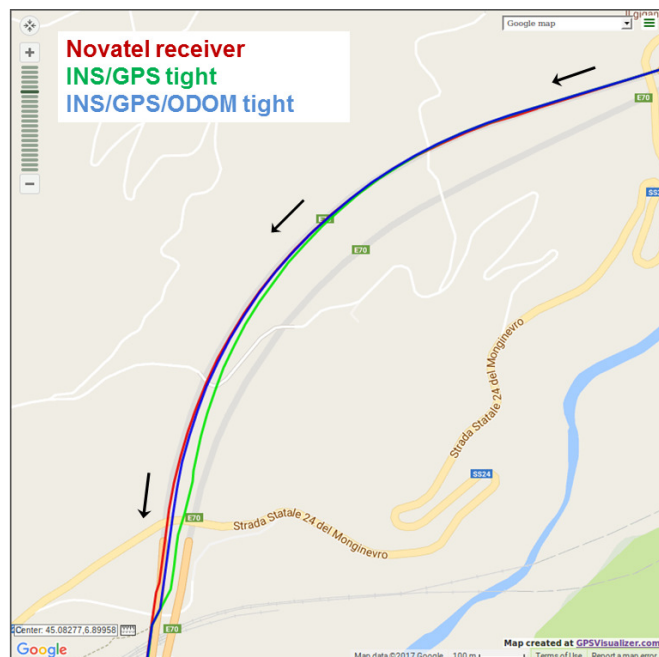

Fig. 16. Comparison of the estimated positions for the tunnel #5.

Fig. 16 reports the positions along the tunnel #5, which is approximately 1 km long. The red line indicates the positions computed by the Novatel SPAN-CPT, the green is used for the first RPU and the blue is for the second RPU processing also data from the odometer. Arrows indicate the driving direction.
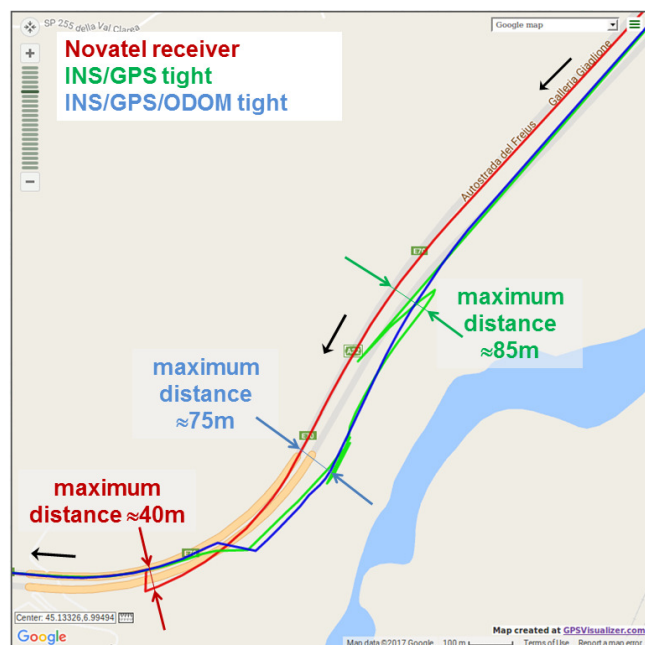

Fig. 17. Comparison of the estimated positions for the tunnel #2.

It can be noticed that the estimated paths are almost coincident until half of the tunnel for all the three devices, whereas at the end of the tunnel it is possible to observe a cross-track horizontal position error of approximately 40 m with the first RPU, featuring INS/GPS tight integration only.

Fig. 17 and Fig. 18 show the positions evaluated during longer outages, in bending road tunnels 2.55 km and 5.32 km long. At an average speed of 70 km/h, these obscured the GNSS signals for more than 2 and 4.5 minutes, respectively. In both cases, we can clearly observe how the positions provided by both the RPUs and the Novatel SPAN-CPT are affected by relevant cross-track errors, when compared with the reference map, especially at the end of the tunnel. Indeed, out of the tunnel #2 (Fig. 17) the maximum distance estimated between the reference point on the map and the position provided by the Novatel SPAN-CPT is approximately 40 m. The first RPU showed also along track errors, with a maximum cross-track error equal to 85 m. The data from the odometer helped to have a smoother estimate of the trajectory, with negligible along-track errors and a lower maximum cross-track error (i.e.: 75 m) with respect to the first RPU.
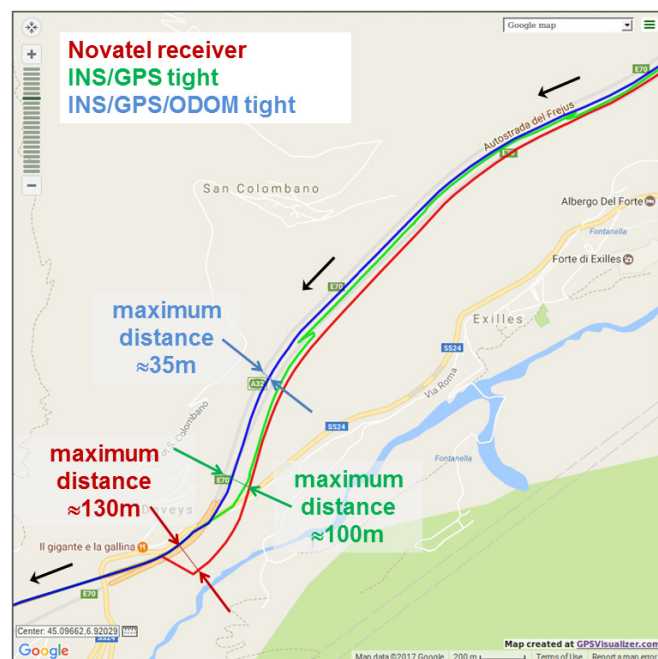

Fig. 18. Comparison of the estimated positions for tunnel #4.

During the test performed in the tunnel #4, the second RPU showed a maximum cross-track error of 35 m. When the odometer is disabled, the tight integration error increases up to 100 m, and reaches 130 m even with the Novatel SPAN-CPT. Despite it is a "survey-grade" receiver, combined with a tactical-grade inertial sensor, it experiences significant position errors, caused by some minutes of GPS signal outages due to the tunnel. In this harsh environment, the RPU outperforms the Novatel SPAN-CPT, especially if odometer data is integrated. Such results confirm that tightly coupled architectures can provide significant advantages, even using low cost sensors and consumer-grade GNSS receivers. This provided that additional constraints, logical controls and countermeasures to the in-run variations of the IMU noises are implemented. Indeed, it is possible to design hybrid positioning systems suitable for land navigation at moderated

cost, with performance comparable to that of professional equipment.

For the sake of completeness, in order to compare the performance of the two RPUs, the maximum cross-track error with respect to the reference map has been measured, with a resolution of 5 m, for each tunnel highlighted in Fig. 15.a and in Fig. 15.b, respectively. Results are reported in Table 3 where the length of each tunnel is also indicated.

TABLE III
MAXIMUM CROSS-TRACK ERROR IN CASE OF LONG GPS OUTAGE.

Tunnel index	Tunnel length		Cross-Track Error [m]	
	[s]	[km]	RPU 1 (INS/ GPS)	RPU 2 (INS/ GPS/ ODOM)
1	35	1.15	90	40
2	95	2.55	85	75
3	65	1.40	25	15
4	190	5.32	100	35
5	55	1.60	40	10
6	95	1.29	15	15
7	115	2.20	25	20
8	65	1.34	35	40
9	50	1.60	10	10
10	190	5.18	50	35
11	50	1.40	200	20
12	90	2.64	50	35

Values in Table 3 further motivate the use of the odometer, when this can be integrated in the positioning system of the vehicle. The advantage is quite evident in tunnels #4 and #11 where the error is of only 35 m and 20 m when the odometer is used, compared to the 100 m and 200 m when the speed sensor is disabled. As a figure of merit, the cross-track position error is reduced, on average, of 46% when the odometer is enabled in the tight integration algorithm.

The highest error with the second RPU is of about 75 m and was measured at the end of the tunnel #2, even if such tunnel was not the longest one in our test campaign. We probed the reason of such large position error and we identified the origin. It was because the tunnel #2 was encountered only a few seconds later the car drive test started, and such short amount of time prevented the tight algorithm to fully recover the initial heading error of the IMU.

V. CONCLUSION

This paper presented the design of a positioning system based on tightly coupled sensors, namely a consumer-grade GPS receiver, a low-cost IMU and a car odometer. After recalling the mathematical model at the basis of the tight integration, the paper described add-on algorithms necessary to achieve a real-time implementation on an embedded system. These additional algorithms remarkably improve the performance of the integrated system with respect to a traditional tightly-coupled method. From a computational load point of view, these additions do not require high demanding computing resources since they only involve the low-rate part of the INS tight integration. The paper reported the

performance of the developed system, which was stressed in different environmental conditions and characterized through the statistical analysis of the horizontal position errors before map-matching. Whereas in open sky conditions, standalone multi-constellation GNSS receivers already provide position accuracy within the lane width, in urban contexts a multiple sensors tightly coupled solution is needed to significantly reduce the position errors. According to the analysis reported in the paper, mainly the 95th percentile is reduced. In real systems, such a reduction allows the map-matching algorithm to recover almost completely the final positioning error. Furthermore, we observed improved performance in a mountain region, with frequent GNSS signal outages due to consecutive tunnels. In such a scenario, the positioning system under test had performance comparable to the one provided by a professional equipment, composed by a survey-grade GPS receiver and combined with a tactical-grade IMU. This result paves the ways to further developments, as it shows that even extremely low-cost sensors can match the requirements of new demanding road applications, when they are tightly coupled together. Examples include pay-as-you-drive insurances, tracking of fleet for winter road maintenance, automated systems for advanced driver assistance and autonomous vehicles. In the years ahead, the improvement of Micro Electrical Mechanical Sensors (MEMS) technology and the further evolution of GNSS, with enhanced signal formats, different frequency bands and more satellites in view, are expected to further increase the positioning performance of mass-market devices, enabling a variety of new services for road users. The combination of low cost positioning sensors will have a key-role also in applications requiring centimeter levels accuracy, but where the use of digital maps is not possible. Examples include precision farming and systems for autonomous machine guidance in agriculture.

APPENDIX I- INS ERROR MODEL AND INS/GPS STATE TRANSITION MATRIX

A theoretically rigorous error model for an accelerometer and gyroscope can be found in [46]. In order to reduce the complexity of such model and guarantee the stability and observability of each state in the KF, both sensors' errors are considered composed of a bias term and noise, with some temporal variability given to the bias states. The temporal variability is used to account for time-varying effects in the theoretical models described above, such as temperature sensitivity, scale factors, etc. [11]. As a consequence, $\delta\mathbf{f}^b$ and $\delta\boldsymbol{\omega}^b$ can be expressed as in (II.1):

$$\delta\mathbf{f}^b = \delta\mathbf{k} + \mathbf{w}_f$$
$$\delta\boldsymbol{\omega}^b = \delta\mathbf{d} + \mathbf{w}_\omega$$
(II.1)

where $\delta\mathbf{k}$, $\delta\mathbf{d}$ are the bias drifts of the accelerometers and gyroscopes sensors, and $\mathbf{w}_f$, $\mathbf{w}_\omega$ are the noise components that affect the two types of INS sensors, respectively. The KF

is only in charge of estimating the drift components of the biases since their deterministic part is typically estimated offline in case of accelerometers (one common technique suitable for low-cost IMU is described in [47]) or is evaluated in real-time for the gyroscopes by keeping the IMU in static for a predefined amount of time.

Thus, equation (2) can be rewritten to comprise a continuous-time expression of a system error model suitable for an INS/GPS tight integration. According to [11], we have:

$$
\begin{bmatrix}
\delta \dot{\mathbf{r}}^e_{3\times1} \\
\delta \dot{\mathbf{v}}^e_{3\times1} \\
\delta \dot{\mathbf{A}}^e_{3\times1} \\
\delta \ddot{\mathbf{r}}^b_{3\times1} \\
\delta \dot{\boldsymbol{\omega}}^b_{3\times1} \\
\delta \dot{b}_r \\
\delta \dot{d}_r
\end{bmatrix}
=
\underbrace{
\begin{bmatrix}
\mathbf{0}_{3\times3} & \mathbf{I}_{3\times3} & \mathbf{0}_{3\times3} & \mathbf{0}_{3\times3} & \mathbf{0}_{3\times3} & \mathbf{0}_{3\times1} & \mathbf{0}_{3\times1} \\
\mathbf{N}^e_{3\times3} & -2\boldsymbol{\Omega}^e_{ie,3\times3} & -\mathbf{F}^e_{3\times3} & \mathbf{R}^e_{b,3\times3} & \mathbf{0}_{3\times3} & \mathbf{0}_{3\times1} & \mathbf{0}_{3\times1} \\
\mathbf{0}_{3\times3} & \mathbf{0}_{3\times3} & -\boldsymbol{\Omega}^e_{ie,3\times3} & \mathbf{0}_{3\times3} & \mathbf{R}^e_{b,3\times3} & \mathbf{0}_{3\times1} & \mathbf{0}_{3\times1} \\
\mathbf{0}_{3\times3} & \mathbf{0}_{3\times3} & \mathbf{0}_{3\times3} & -diag(\boldsymbol{\alpha}_{1\times3}) & \mathbf{0}_{3\times3} & \mathbf{0}_{3\times1} & \mathbf{0}_{3\times1} \\
\mathbf{0}_{3\times3} & \mathbf{0}_{3\times3} & \mathbf{0}_{3\times3} & \mathbf{0}_{3\times3} & -diag(\boldsymbol{\beta}_{1\times3}) & \mathbf{0}_{3\times1} & \mathbf{0}_{3\times1} \\
\mathbf{0}_{1\times3} & \mathbf{0}_{1\times3} & \mathbf{0}_{1\times3} & \mathbf{0}_{1\times3} & \mathbf{0}_{1\times3} & 0 & 1 \\
\mathbf{0}_{1\times3} & \mathbf{0}_{1\times3} & \mathbf{0}_{1\times3} & \mathbf{0}_{1\times3} & \mathbf{0}_{1\times3} & 0 & 0
\end{bmatrix}
}_{\mathbf{F}}
\cdot
\underbrace{
\begin{bmatrix}
\delta \mathbf{r}^e_{3\times1} \\
\delta \mathbf{v}^e_{3\times1} \\
\delta \mathbf{A}^e_{3\times1} \\
\delta \dot{\mathbf{r}}^b_{3\times1} \\
\delta \boldsymbol{\omega}^b_{3\times1} \\
\delta b_r \\
\delta d_r
\end{bmatrix}
}_{\delta\mathbf{x}}
+
\underbrace{
\begin{bmatrix}
\mathbf{0}_{3\times3} & \mathbf{0}_{3\times3} & \mathbf{0}_{3\times3} & \mathbf{0}_{3\times3} & \mathbf{0}_{3\times1} & \mathbf{0}_{3\times1} \\
\mathbf{R}^e_{b,3\times3} & \mathbf{0}_{3\times3} & \mathbf{0}_{3\times3} & \mathbf{0}_{3\times3} & \mathbf{0}_{3\times1} & \mathbf{0}_{3\times1} \\
\mathbf{0}_{3\times3} & \mathbf{R}^e_{b,3\times3} & \mathbf{0}_{3\times3} & \mathbf{0}_{3\times3} & \mathbf{0}_{3\times1} & \mathbf{0}_{3\times1} \\
\mathbf{0}_{3\times3} & \mathbf{0}_{3\times3} & \mathbf{I}_{3\times3} & \mathbf{0}_{3\times3} & \mathbf{0}_{3\times1} & \mathbf{0}_{3\times1} \\
\mathbf{0}_{3\times3} & \mathbf{0}_{3\times3} & \mathbf{0}_{3\times3} & \mathbf{I}_{3\times3} & \mathbf{0}_{3\times1} & \mathbf{0}_{3\times1} \\
\mathbf{0}_{1\times3} & \mathbf{0}_{1\times3} & \mathbf{0}_{1\times3} & \mathbf{0}_{1\times3} & 1 & 0 \\
\mathbf{0}_{1\times3} & \mathbf{0}_{1\times3} & \mathbf{0}_{1\times3} & \mathbf{0}_{1\times3} & 0 & 1
\end{bmatrix}
}_{\mathbf{G}}
\cdot
\underbrace{
\begin{bmatrix}
\mathbf{w}_{f,3\times1} \\
\mathbf{w}_{\omega,3\times1} \\
\mathbf{w}_{\delta k,3\times1} \\
\mathbf{w}_{\delta l,3\times1} \\
w_{b_r} \\
w_{b_r}
\end{bmatrix}
}_{\mathbf{W}}
\qquad \text{(II.2)}
$$

where

$\mathbf{I}_{3\times3}$ is the unit matrix;

$\mathbf{N}_{3\times3}^{e}$ is the tensor of gravity gradients expressed in ECEF frame according to [11];

$\mathbf{\Omega}_{ie,3\times3}^{e}$ is the skew-symmetric matrix of the rotation rate ω_{e} of the Earth expressed in ECEF frame;

$\mathbf{F}_{3\times3}^{e}$ is the skew-symmetric matrix of the accelerometers forces in ECEF frame;

$\mathbf{R}_{b,3\times3}^{e}$ is direction cosine matrix from the body frame 'b' to ECEF frame 'e';

$\mathbf{\alpha}_{1\times3}$ represents the vector of time constants related to the Gauss-Markov noises of the triaxial accelerometers;

$\mathbf{\beta}_{1\times3}$ represents the diagonal matrix of time constants related to the Gauss-Markov noises of the triaxial gyroscopes;

$\mathbf{w}_{f,3\times1}$ is the noise component that affects the accelerometers as stated in (II.1);

$\mathbf{w}_{\omega,3\times1}$ is the noise component that affects the gyroscopes as stated in (II.1);

$\mathbf{w}_{\delta k,3\times1}$ is the Gauss-Markov process driving noise used to model the accelerometers bias drift;

$\mathbf{w}_{\delta d,3\times1}$ is the Gauss-Markov process driving noise used to model the gyroscopes bias drift;

$w_{b_{r}}$ is the noise of the receiver's clock bias;

$w_{\dot{b}_{r}}$ is the noise of the receiver's clock drift;

$\mathbf{F}$ is the whole matrix of the system model;
$\mathbf{G}$ is the matrix that relates the states with noise sources.

For most system models the dynamics matrix $\mathbf{F}$ can be considered time invariant for the time interval over which the KF prediction is performed [11]. The benefit is that, under this assumption, the transition matrix $\mathbf{\Phi}_{k|k-1}$ of a discrete-time Kalman filter can be obtained as the solution of the system model in the absence of forcing functions, given by (II.3) according to [48]:

$$\mathbf{\Phi}_{k|k-1} = e^{\mathbf{F}\cdot dt} \qquad\qquad \text{(II.3)}$$

where dt is the time interval over which the prediction is performed.

The exponential function of (II.3) can be linearized in case of Extended Kalman Filter (EKF) by using the first order terms in the Taylor series:

$$e^{\mathbf{F}\cdot dt} = \mathbf{I} + \mathbf{F}\cdot dt + \frac{(\mathbf{F}\cdot dt)^{2}}{2} + \mathrm{O}(3) \qquad \text{(II.4)}$$

where $\mathrm{O}(3)$ denotes terms of order 3. The process noise matrix of a discrete-time KF, that we indicate with $\mathbf{Q}_{k}$, can be calculated through numerical integrations. In [48] one possible solution is described, and this method is typically adopted for multi sensors fusion applications, as in case of INS/GPS integration. According to [48], $\mathbf{Q}_{k}$ can be written as:

$$\mathbf{Q}_{k} = \left(\mathbf{\Phi}_{k|k-1}\mathbf{G}_{k}\mathbf{Q}_{c}\mathbf{G}_{k}^{T}\mathbf{\Phi}_{k|k-1}^{T} + \mathbf{G}_{k}\mathbf{Q}_{c}\mathbf{G}_{k}^{T}\right)\frac{dt}{2} \qquad \text{(II.5)}$$

where $\mathbf{Q}_{c}$ is the continuous-time spectral density matrix of the forcing functions and superscript T is used to specify the matrix transpose.

APPENDIX II- INS/GPS TIGHTLY COUPLED DESIGN MATRIX COMPUTATION

As far as the measurements update of the KF is concerned, the function of (3) can be tailored for the tightly coupled INS/GPS integration as in (III.1):

$$\underbrace{\begin{bmatrix} \mathbf{\rho}_{k,INS} - \mathbf{\rho}_{k,GPS} \\ \dot{\mathbf{\rho}}_{k,INS} - \dot{\mathbf{\rho}}_{k,GPS} \end{bmatrix}}_{\mathbf{Z}_{k}} = \underbrace{\begin{bmatrix} \mathbf{H}_{\rho,N\times3} & \mathbf{0}_{N\times3} & \mathbf{0}_{N\times9} & \mathbf{1}_{N\times1} & \mathbf{0}_{N\times1} \\ \mathbf{0}_{N\times3} & \mathbf{H}_{\rho,N\times3} & \mathbf{0}_{N\times3} & \mathbf{0}_{N\times1} & \mathbf{1}_{N\times1} \end{bmatrix}}_{\mathbf{H}_{k}} \cdot \delta\mathbf{x}_{k,17\times1} + \mathbf{v}_{k} \qquad \text{(III.1)}$$

where $\mathbf{H}_{\rho,N\times3}$ is the matrix that relates the measurements to the error states and with the subscript N we indicate the number of satellites in view at the k-th time instant. Since the relationship between $\mathbf{Z}_{k}$ and $\delta\mathbf{x}$ vectors is non-linear, a first order Taylor expansion is used in case of EKF and (3) can be rewritten as:

$$\begin{aligned} \mathbf{z}_{k} &= h(\mathbf{x}_{k}) + \mathbf{v}_{k} \\ &\approx h(\mathbf{x}_{k}) + \frac{\delta h(\mathbf{x}_{k})}{\delta\mathbf{x}_{k}}\delta\mathbf{x}_{k} + \mathbf{v}_{k} \end{aligned} \qquad \text{(III.2)}$$

Thus, the Jacobian matrix of $\mathbf{H}_{\rho,N\times3}$ can be computed as:

$$\mathbf{H}_{\boldsymbol{\rho},N\times 3} = \begin{bmatrix} \dfrac{\breve{x}-x_1}{d_1} & \dfrac{\breve{y}-y_1}{d_1} & \dfrac{\breve{z}-z_1}{d_1} \\ \dfrac{\breve{x}-x_2}{d_2} & \dfrac{\breve{y}-y_2}{d_2} & \dfrac{\breve{z}-z_2}{d_2} \\ \vdots & \vdots & \vdots \\ \dfrac{\breve{x}-x_N}{d_N} & \dfrac{\breve{y}-y_N}{d_N} & \dfrac{\breve{z}-z_N}{d_N} \end{bmatrix} \qquad \text{(III.3)}$$

where $[\breve{x},\breve{y},\breve{z}]$ is the vector of the estimated user's position coordinates, $[x_{1\cdots N}, y_{1\cdots N}, z_{1\cdots N}]$ represents the N satellites positions in ECEF frame, and $d_{1,\dots,N}$ is the norm of the geometric distance between the GPS receiver and N-th satellite.

In case of a standalone, single frequency GPS receiver, the noise vector $\mathbf{v}_k$ has a Gaussian distribution as stated in (III.4):

$$\mathbf{v}_k \sim N(\mathbf{0},\mathbf{R}_{\mathbf{v}_k}) \qquad \text{(III.4)}$$

where the covariance matrix $\mathbf{R}_{\mathbf{v}_k}$ is a diagonal one, since the noise related to each satellite can be considered statistically independent

REFERENCES

[1] S. Carcanague, O. Julien, W. Vigneau, C. Macabiau, and G. Hein, "Finding the right algorithm: Low-cost, single-frequency GPS/GLONASS RTK for road users," *Inside GNSS*, vol. 8, no. 6, pp. 70–80, Dec. 2013.

[2] A. Defina, A. Favenza, G. Falco, D. Orgiazzi, and M. Pini, "ASSIST: An Advanced Snow Plough and Salt Spreader Based on Innovative Space Based Technologies," in *Proc. ION GNSS,* Tampa, FL, USA, Sept. 2015, pp. 2041–2054.

[3] S. Godha, and E.Cannon., "GPS/MEMS INS integrated system for navigation in urban areas,". *GPS Solutions*, vol. 11, no. 3, pp. 193–203, Jul. 2007.

[4] D.M. Bevly, and S. Cobb, *GNSS for Vehicle Control*; Artech House Publishers: Boston, MA, USA, 2009.

[5] D.H. Titterton, and J.L. Weston, *Strapdown Inertial Navigation Technology,* 2nd ed.; American Institute of Aeronautics and Astronautics: Reston, VA, USA, 2004.

[6] P. Aggarwal, Z. Syed, A. Noureldin, and N. El-Sheimy, *MEMS-Based Integrated Navigation*; Artech House Publisher: Norwood, UK, 2010.

[7] M. Shafiq, "GNSS/INS Integration in Urban Areas," Ph.D. Thesis, Norwegian University of Science and Technology, Trondheim, Norway, Apr. 2014.

[8] Y. Gao, S. Liu, M. Atia Mohamed, and A. Noureldin, "INS/GPS/LiDAR Integrated Navigation System for Urban and Indoor Environments Using Hybrid Scan Matching Algorithm," *Sensors*, vol. 15, pp. 23286–23306, Sept 2015.

[9] J.F. Wagner, and T. Wieneke, "Integrating satellite and inertial navigation-conventional and new fusion approaches," *Control Eng. Pract.*, vol. 11, no 5, pp. 543–550, May 2003.

[10] A. Solimeno, "Low-Cost INS/GPS Data Fusion with Extended Kalman Filter for Airborne Applications," Master's Thesis, Universidad Tecnica de Lisboa, Lisbon, Portugal, Jul. 2007.

[11] M. Petovello, "Real-time Integration of a Tactical-Grade IMU and GPS for High-Accuracy Positioning and Navigation," PhD Thesis, Dept of Geomatics Eng., University of Calgary, Canada, UCGE Report No. 20173, Apr. 2003.

[12] A. Soloviev, F. Van Graas, and S. Gunawardena, "Implementation of Deeply Integrated GPS/LowCost IMU for Acquisition and Tracking of Low CNR GPS Signals," in *Proc. ION National Technical Meeting (NTM) GNSS*, San Diego, CA, USA, Jan. 2004; pp. 923–935.

[13] G. Gao, and G. Lachapelle, "A Novel Architecture for Ultra-Tight HSGPS-INS Integration," *J. Global Position. Syst*, vol.7, no.1, pp.46–61, Jan. 2008.

[14] F. Diggelen, C. Abraham, "Indoor GPS Technology", Global Locate, Inc., San Jose, CA. [Online]. Available: http://www.globallocate.com/SEMICONDUCTORS/Semi_Libr_Piece/Ind oorGPSTechnology.pdf.

[15] D.E. Lewis, "Ultra-Tightly Coupled GPS/INS Tracking Performance," in *Proc. ATIO*, Forum, Denver, CO, USA. 17–19 November 2003, pp. 1–7.

[16] M Lashley. and D.M Bevly. "A Comparison of the Performance of a Non-Coherent Deeply Integrated Navigation Algorithm and a Tightly Coupled Navigation Algorithm," n *Proc. ION GNSS*, Savannah, GA, USA, 16–19 September 2008; pp. 2123–2129.

[17] J. Georgy, A. Noureldin, M. J. Korenberg, and M. M. Bayoumi, "Low-Cost Three-Dimensional Navigation Solution for RISS/GPS Integration Using Mixture Particle Filter," *IEEE Trans. Veh. Technol,* vol. 59, no.2, pp. 599–615, Feb. 2010.

[18] S. Julier, J. Uhlmann,, and , H. G Durrant-Whyte, ".A new method for the nonlinear transformation of means and covariances in filters and estimators," *IEEE Trans. Aut. Control*, vol. 45, no. 3, pp. 477–482, Mar. 2000.

[19] U. Iqbal, J. Georgy, and Walid F. Abdelfatah, "Pseudoranges Error Correction in Partial GPS Outages for a Nonlinear Tightly Coupled Integrated System," *IEEE Trans. Veh. Technol,* vol. 14, no. 3, pp. 1510–1524, Sept. 2013.

[20] J. Georgy, "Advanced nonlinear techniques for low cost land vehicle navigation," Ph.D. thesis, Dept. Elect. Comput. Eng., Queen's Univ., Kingston, ON, Canada, 2010.

[21] W. Abdel-Hamid, A. Noureldin, and N. El-Sheimy, "Adaptive fuzzy prediction of low-cost inertial-based positioning errors," *IEEE Trans. Fuzzy Syst*., vol. 15, no. 3, pp. 519–529, Jun. 2007.

[22] R. Sharaf and A. Noureldin, "Sensor integration for satellite-based vehicular navigation using neural networks," *IEEE Trans. Neural. Netw.* vol. 18, no. 2, pp. 589–594, Mar. 2007.

[23] R. Sharaf, A. Noureldin, A. Osman, and N. El-Sheimy, "Online INS/GPS integration with a radial basis function neural network," *IEEE Aerosp. Electron. Syst. Mag*., vol. 20, no. 3, pp. 8–14, Mar. 2005.

[24] Q. Xu, X. Li, B. Li, X. Song, and Zhixiang Cai, "A Reliable Hybrid Positioning Methodology for Land Vehicles Using Low-Cost Sensors," *IEEE Trans. Int. Ttransp. Syst.,* vol. 17, no.3, pp. 834–847, Mar. 2016.

[25] H. Hur, and H. Ahn, "Discrete-time H∞ filtering for mobile robot localization using wireless sensor network," *IEEE Sensors*, vol. 13, no. 1, pp. 245–252, Jan. 2013.

[26] C. Hide, and T. Moore, "GPS and Low Cost INS Integration for Positioning in the Urban Environment," In *Proc. ION GNSS*, Long Beach, CA, USA, Sept. 2005; pp. 1007–1015.

[27] G. Falco, G.A Einicke, J.T. Malos, and F. Dovis, "Performance analysis of constrained loosely coupled GPS/INS integration solutions," *Sensors*, vol. 12, no.11, pp: 15983–16007, Nov. 2012.

[28] L.N. Hieu, and V.H. Nguyen, "Loosely Coupled GPS/INS Integration with Kalman filtering for land vehicle applications," In *Proc. ICCAIS*, Ho Chi Minh City, Vietnam, Nov. 2012; pp. 90–95.

[29] Y. Tawk, P. Tomé, C. Botteron, Y. Stebler, and P.-A. Farine, "Implementation and Performance of a GPS/INS Tightly Coupled Assisted PLL Architecture Using MEMS Inertial Sensors," *Sensors*, vol. 14, no.2, pp: 3768–3796, Feb. 2014.

[30] G. J. Geier, "GPS Integration with Low Cost Sensor Technology for Automotive Applications", ENGO 699.47 Lecture Notes, Dept. Geomatics Eng., University of Calgary, August 1998.

[31] R. G. Brown and P. Y. C. Hwang, *Introduction to Random Signals and Applied Kalman Filtering: With MATLAB Exercises and Solutions,* 3rd ed. New York: Wiley, 1997.

[32] M. S. Grewal and A. P. Andrews*, Kalman Filtering: Theory and PracticeUsing MATLAB,* 2nd ed. New York: Wiley, 2001.

[33] D. Simon*, "*Kalman Filtering," *Embedded Syst. Program.,* vol. 14, no. 6, pp. 72–79, Jun. 2001.

[34] D. Obradovic, H. Lenz, and M. Schupfner, "Fusion of sensor data in Siemens car navigation system,*" IEEE Trans. Veh. Technol*., vol. 56, no. 1, pp. 43–50, Jan. 2007.

[35] J. Georgy and A. Noureldin, "Tightly coupled low cost 3D RISS/GPS integrationusing a mixture particle filter for vehicular navigation," *Sensors*, vol. 11, no. 4, pp. 4244–4276, Apr. 2011.

[36] A. Soloviev, "Tight Coupling of GPS, INS, and Laser for Urban Navigation," *IEEE Trans. Aerosp. Electron. Syst,* vol. 46, no. 4, pp. 1731–1746, Oct. 2010

[37] I. Miller, and M. Campbell, "Sensitivity Analysis of aTightly-Coupled GPS/INS System for Autonomous Navigation,"*IEEE Trans. Aerosp. Electron. Syst,* vol. 48, no. 2, pp. 1115–1135, Apr. 2012.

[38] M. George, and S. Sukkarieh,, "Tightly coupled INS/GPS with bias estimation for UAV applications," *in Proc. Australasian Conferences on Robotics and Automation*, Sidney, Australia, Dec. 2005.

[39] I. Miller, et al, "Tightly-coupled GPS/INS system design for autonomous urban navigation,*",in Proc IEEE/ION Position, Location and Navigation Symposium,* Monterey, CA, USA, 2008, pp. 1297—1310.

[40] .G. Falco, E. López Serna, F. Zacchello,, and S. Bories,. "Low-cost Real-time Tightly-coupled GNSS/INS Navigation System Based on Carrier Phase Double Differences for UAV Applications," in *Proc. ION GNSS,* Tampa, FL, USA, 2014, pp.:841-857.

[41] H. Liu, S. Nassar, and N. El-Sheimy, "Two-Filter Smoothing for Accurate INS/GPSLand-Vehicle Navigation in Urban Centers," *IEEE Trans. Veh. Technol,* vol. 59, no.9, pp. 4256–4267, Nov. 2010.

[42] J. Gao, M. G. Petovello, and M. E. Cannon, "GPS/Low-Cost IMU/Onboard Vehicle Sensors Integrated Land Vehicle Positioning System," *J. on Embedded Syst*. Vol. 2007, no. 62616, pp. 1-20, Apr. 2007.

[43] S.Y.Cho, "IM-Filter for INS/GPS-Integrated Navigation System Containing Low-Cost Gyros," *IEEE Trans. Aerosp. Electron. Syst,* vol. 50, no. 4, pp. 2619-2629, Oct. 2014.

[44] B. M Scherzinger, "Inertial navigator error models for large heading uncertainty," in *Proc. IEEE PLANS*, Atlanta, GA, USA, April 1996, pp.:477–484.

[45] A. Kuncar, M. Sysel, and T. Urbanek, "Calibration of Low-Cost Three Axis Magnetometer with Differential Evolution," *Cybernetics and Mathematics Applications in Intelligent Systems*. vol 574, pp. 120-130, Apr. 2017.

[46] C. Jekeli, *Inertial Navigation Systems with Geodetic Application*, New York: Walter de Gruyter, 2000.

[47] E-H Shin, and N. El-Sheimy, "A new calibration method for strapdown inertial navigation systems," *Z. Vermess*. Vol. 127 pp 41–50.

[48] A. Gelb, *Applied Optimal Estimation*, Boston: The M.I.T. Pres, 1974.

[49] Invense, 2010. ITG-3200 Product Specification. [online] Available at: <www.invensense.com/mems/gyro/itg3200.html> [Accessed on 15 May 2017].

[50] P. D. Groves. *Principles of GNSS, inertial, and multi-sensor Integrated Navigation Systems*. Boston: Artech House, 2008.

[51] K. A. Rahim, "Heading Drift Mitigation for Low-cost Inertial Pedestrian Navigation," PhD Thesis, Geospatial Institute, Nottingham, UK, Mar. 2012.

[52] E. Shin, "Estimation techniques for low-cost inertial navigation," Ph.D. Thesis, Dept of Geomatics Eng., University of Calgary, Canada, UCGE Report No. 20219, May. 2005.

[53] G. Falco, G. Marucco, and M. Pini, "Loose and tight GNSS/INS integrations: comparison of performance assessed in real urban scenarios," *Sensors*, vol. 17, no. 255, pp: 1-25, Jan 2017.

[54] H Kuusniemi, "User-level reliability and quality monitoring in satellite based personal navigation," PhD Thesis, Dept. Geomatics Eng., Tampere University of Technology, Finland, May 2005.

[55] A. Noureldin, T. B. Karamat, M. D. Eberts, and A. El-Shafie, "Performance enhancement of MEMS-based INS/GPS integration for low-cost navigation applications*," IEEE Trans. Veh. Technol*., vol. 58, no. 3, pp. 1077–1096, Mar. 2009.

[56] ETSI TS 103 246-5: Satellite Earth Stations and Systems (SES), GNSS based location systems, Performance Test Specification.

Gianluca Falco is a Communication engineer, currently employed at the Navigation Technologies research area of the Istituto Superiore Mario Boella (ISMB), in Turin, Italy. He received a M.S. in Communications Engineering in 2007 from Politecnico di Torino, Italy. Since 2011, he holds a Ph.D. degree in Electronic and Communication. His interest focuses on multi-sensors fusion, particularly between GPS and inertial navigation systems, as well as on advanced processing techniques for dual frequency and multi-constellation GNSS receivers.

Mario Nicola received the M.S. in Computer Science Engineering from the Politecnico di Torino in 2002. In 2005 he obtained his Ph.D. degree in Electronics and Communications Engineering working on reconfigurable architectures for wireless communication systems.
He is a researcher in the staff of the Navigation Technologies research area at ISMB, Torino. His main activity is the implementation of algorithms for software radio GPS/Galileo receivers.

Marco Pini heads the Navigation Technologies research area at the ISMB. He holds a Ph.D. degree in Electronics and Communications from Politecnico di Torino University.
As a result of the experience gained on GNSS receivers and performance, Marco Pini has been responsible for the R&D activities of several projects. His major interests cover the field of baseband signal processing on new GNSS signals, multi-frequency RF front end design and software radio receivers.